Electronic Supplementary Material (ESI) for Materials Horizons.

Supplementary Materials

This file includes:
Materials and Methods
Supplementary text
Supplementary Tables 1 to Table 2
Supplementary Figures 1 to 10
Video of MDS visualization
References

Materials and Methods:

The nanoscale films were magnetron-sputtered in the co-deposition chamber of a physical vapor deposition system (DCA, Finland)[22] equipped with 5 magnetron cathodes spaced 72° apart in a sputter-down configuration. Each cathode had a Ø4-inch single-element target: Ni (99.995%, K.J. Lesker, USA), Cr (99.99%, Kaistar, USA), Mn (99.95%, Sindlhauser Materials, Germany), Co (99.99%, Sindlhauser), Fe (99.99%, Sindlhauser), with cross-contamination shielding around each cathode having an opening only towards the substrate position. Pre-sharpened Si tip arrays (CAMECA Instruments) and additional substrates were placed at the confocal point with all cathodes tilted by 45°. The target-to-substrate, center-to-center distance was approximately 185 mm. The substrates entered the PVD system through a loadlock, passed through a UHV central handling chamber and then to the deposition chamber (base vacuum 2.8×10^{-5} Pa). To remove adsorbed surface layers, the CPPs can also be heated in vacuum prior to the deposition. Although kept under vacuum, the targets were still first precleaned by sputtering against closed shutters for 300 seconds. The deposition was carried out at a substrate carrier temperature of 25°C at a pressure of 0.67 Pa, and to achieve uniform mixing and conformal coating, the substrate table was rotated at 20 rpm. The powers applied to each target were as follows: 139 W RF to Ni, 68 W DC to Cr, 120 W RF to Mn, 172 W RF to Co and 57 W DC to Fe. The power to each material was initially selected to give equal deposition rates, with the final values being adjusted based on elemental composition measurements by EDX. The EDX average standard deviations were less than 1 at.% or better for each of the elements analyzed. The total deposition rate with these conditions was 0.21 nm/s, yielding a 100-nm layer on a flat reference surface in 460 seconds.

APT coupon temperature during vacuum annealing

The APT coupon with an array of 36 sharpened tips is placed on a Cu carrier, and held in place with a spring clip (Fig. 1a). Together they were held in a Swagelok nut (Fig. 1b), and placed on a stainless steel plate and transferred into a vacuum chamber for annealing. The coupon and its holder were then picked out of the nut and transferred together into the APT for measurements.

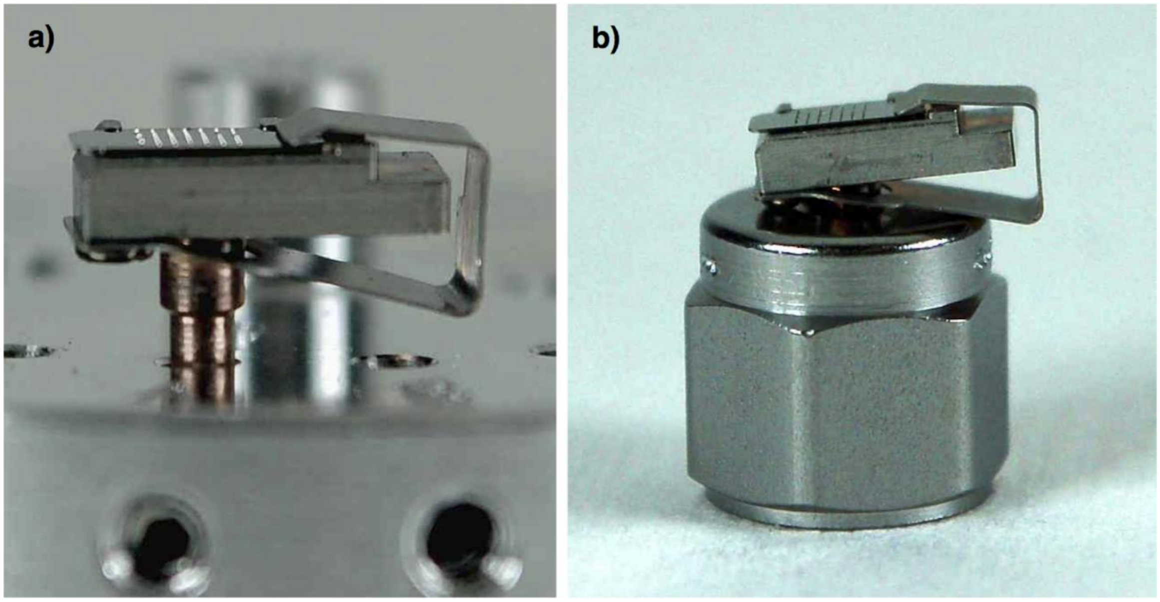

Fig. 1. a) APT coupon held on Cu carrier (also coated) with U-shaped spring clip; b) APT coupon and Cu-carrier placed in a stainless steel nut. This assembly was transported on a stainless steel plate via a loadlock into the UHV chamber for annealing.

However, this carrier arrangement led to a significant deviation from the previous calibration of actual Si-wafer substrate temperature versus heater setpoint controlled temperature, even at high temperatures where radiation is expected to be the dominating heat transfer mechanism. Therefore, several attempts were made to directly measure the actual APT coupon temperature by attaching a thermocouple under the U-shaped spring clip in place of the APT coupon itself. Next, the annealing state of an APT coupon lying directly (no Cu-carrier) in a cavity etched into a Si wafer at a verified wafer temperature (detailed below), was correlated to the same annealing state of the APT coupon – Cu-carrier – stainless steel nut and plate arrangement used earlier. This yielded an approximate agreement with the thermocouple temperature measurements of the APT carrier.

TEM grids were annealed separately with the same conditions, but lying directly on the steel carrier plate. The structures resulting from this thermal treatment were not significantly different from the APT results. It is concluded that the temperatures experienced by TEM and APT specimens were similar.

Heater Temperature Calibration

The silicon carbide element resistance heater is controlled by a type K thermocouple, suspended underneath the element mid-way between it and a set of metallic reflectors. The substrate, normally a Ø100 mm Si wafer, is held by the edges directly above the element mid-way between it and a Mo shutter. For purposes of calibration, a Si wafer with type K thermocouples embedded into it at the center, mid-radius and 8 mm from the edge was used, held and positioned identically to any normal substrate. The temperature indicated by the heater thermocouple and controlled by a proportional – integral – derivative (PID) circuit was monitored with the instrumented wafer over the range of 200° to 400°C. The temperatures recorded for the 3 thermocouple positions were always within 2°C of each other and for stable, setpoint temperatures within 1°C. Tests were conducted in vacuum, with a starting pressure of 1.7×10^{-5} Pa.

Over this temperature range, the measured wafer temperature, T_{wafer}, could be fit with Equation 1 where T_{heater} is the heater thermocouple setpoint temperature.

$$T_{wafer} = 0.816(T_{heater}) + 59.6 \qquad \text{(Equation 1)}$$

For the actual annealing experiments, the APT coupons were held in a flat-bottomed cavity with a depth of approximately 350 µm that was etched into a (100) Si wafer and otherwise identical conditions to the calibration measurements.

The APT analysis was performed with a LEAP 5000 XR™ (CAMECA Instruments). For the annealing study the APT measurements were performed in voltage mode at 75 K. The amplitude of the voltage pulse was 20% of the applied direct-current voltage with a pulse frequency of 200 kHz and a detection rate of 0.3% per pulse. For the oxidation study the APT measurement was performed in laser mode at 75 K with 100 pJ laser energy at a pulse frequency of 250 kHz. Reconstruction of the 3D datasets and the quantitative analysis including concentration and binomial frequency distribution were conducted using IVAS 3.6.14 software. The APT data collected < 2 kV, which contains a Mn-rich cap and/or an oxide layer at the very apex of each Si tip, are not included in analyses due to uncertainty of ion location caused by ion trajectories for voltages < 2 kV[23]. The chemical compositions determined by APT in Supplementary Table 1 are averaged values over the whole detected volumes for the states S_1-S_5 at which the decomposition of the single-phase Cantor alloy has not occurred. For S_6 and S_7 the average values are determined from the data in the plateaus of the concentration profiles for each phase shown in Figs. 4**b** and **d.** For the analysis of binomial distributions of alloy elements, the oxide layer (the first 2-3 nm layer in each reconstructed 3D volume) is not considered. For atom maps shown in Figs. 3, 4, Supplementary Figs. 4 and 7 the sectional data-cuts (3 nm slices) are used to visualize the nanoscale grain structure and phases, which would not otherwise be visible due to overlaps of grains/phases from the projection of the 3D structure into 2D images.

TEM investigations were performed using a Tecnai Supertwin F20 G2 operating at 200 kV. Structural information about the forming phases was derived using different methods; first, by measuring interplanar distances on selected area electron diffraction patterns (see Fig. 5, Supplementary Figs.2 and 6); second, by analyzing rotationally averaged patterns, if the number and distribution of the diffracted spots did not allow for unambiguous measurements; third, by analyzing the fast Fourier transform (FFT) of high-resolution TEM (HR-TEM) images. The crystal references used in this study were taken from the inorganic crystal structure database (ICSD): Mn_3O_4_ICSD_77478, Cr_2O_3_ICSD_167291, B2_FeCo_ICSD_155839, Cr_bcc_ICSD_1534885, FeNi_$L1_0$_ICSD_190821 and σ phase_Cr9.32 Fe15.52 Mn0.37 Mo2.21 Ni2.6 _ICSD_102756. For the Cantor phase the fcc lattice constant of 0.36 nm was chosen[21]. For the detailed analyses of the diffraction patterns, the measured interplanar distances were compared to the reference data and small positive deviations were considered, indicating a lattice expansion. As signals from different phases overlap, the individual phases were included one by one in the analysis (Supplementary Table 2). A new phase was therefore introduced only when the already present phases could not account for all measured d_{hkl} distances and/or the APT results indicated occurrence of a new phase.

Overall elemental composition analysis was performed using a SEM (JEOL 5800) equipped with an EDX detector (Inca X-act, Oxford Instruments) on films deposited on (100) Si with a 1.5 µm thermal oxide barrier layer, that were included with each CPP deposition and subsequently treated with identical annealing steps. Data was measured at 20 kV, 600x magnification, a working distance of 10 mm and normalized with a pure Co standard.

Oxidation of a CPP was performed in an air furnace (Nabertherm). Before oxidation, a coated tip array was first subjected to annealing at 100°C for 2.5 h and additional annealing at 150°C for 5 h in vacuum, i.e. directly comparable with annealed but unoxidized material. APT analysis confirmed that the coated thin film in this annealed state remained single-phase Cantor alloy. The tip array was then inserted to the pre-heated (500°C) furnace for a holding time of 5 min followed by cooling in air (about 30 min) before returning to the APT for re-analysis. All post-processing is schematically displayed in Supplementary Fig. 2.

Methodology of visualizing a region-of-interest-amended multinary composition space using multidimensional scaling (MDS)

As soon as >4 dimensional data sets are obtained, there is a challenge in visualization in a low(er) dimensional representation. A shortcoming of methods such as radial visualization (RadViz[21]) is that the projection of a complete quinary space to four dimensions and then further onto two dimensions makes it inherently difficult to deduce iso-elemental trends. The reason is that the iso-elemental areas change shape at different compositions, e.g. the iso $A_{90\text{ at.\%}}$ ‘line’ resembles a pentagon, but the iso $A_{50\text{ at.\%}}$ ‘line’ is an area covering about one third of the diagram (Supplementary Fig. 9). We therefore propose to alleviate the problem of too much data reduction by using metric multidimensional scaling (MDS)[22] in a 3D visualization.

Several other methods can represent high-dimensional data in lower dimensions, such as principal component analysis (PCA) or star plots. In this study, MDS from the scikit-learn library[23] is chosen for dimensionality reduction because the property of interest is the similarity/dissimilarity of compositions. This is readily visualized by the distance of a compositional data point from all others. The dissimilarity metric used is the Euclidean (L2) metric, with the MDS being optimized using the “stress” loss criterion[23]. MDS visualization for CCMs uses the complete quinary composition space at fixed compositional spacing intervals that serve as anchor/orientation points later. The visualization for five elements was chosen to have a discretization step, n, of 10 at.% (i.e. n=10 steps). Using this step size, it is possible to perform the MDS in a reasonable amount of time, since the number of quinary space reference points generated grows with n^4 and the corresponding computational time grows with $(n^4)^3$. Subsequently the approximately 200 experimentally determined compositions from all processing states in this study were added to the 10^4 points from the discretized complete quinary. This step does not significantly enlarge the dataset for the MDS calculations. The resulting 3D MDS is then color-coded such that the compositions belonging to the identified phases are grouped, allowing for the deduction of qualitative trends.

The benefit of MDS over e.g. PCA is that points close to each other in the visualization are also ‘compositionally close’. The points with the highest elemental composition (e.g. pure Cr) are denoted with the corresponding elemental label (‘Cr’). Using this visualization, iso-elemental sections are (mostly) points on a plane at roughly equal distance from a given reference. A generic visualization of iso-elemental sections contrasting RadViz and MDS is shown in Supplementary Fig. 9a-d. As a further comparison to the MDS visualization, the data shown in Fig. 7 is shown as a RadViz visualization in Supplementary Fig. 10a-c. While RadViz is seemingly easier to assess, understanding and interpreting trends is hindered by the fact that iso-elemental cuts change shape in non-evident ways depending on the amount of the chosen element, i.e. $Cr_{10at.\%}$ has a different shape than $Cr_{50at.\%}$.

The methodology of creating an MDS for six elements (senary composition) is similar, but the number of points created by discretizing the complete senary now grows with n^5. Thus, steps of 20 at.% were chosen (n=5 steps) to reduce the calculation time. Also, the 5D projection from a senary composition space results in even more complications in interpreting a RadViz diagram than already found for the 4D projection from a quinary, which is why this alternative visualization is not shown.

Table 1. Average chemical compositions (at.%) of phases detected in the deposited films after all annealing states as determined by APT on the CPP. The values of the as-deposited state were determined by EDX in SEM on a thin film on a flat substrate which was deposited at the same time as the CPP.

State	Phase	Cr	Mn	Fe	Co	Ni
S_0: as-deposited	nanocrystalline Cantor phase	19.4	18.1	20.5	20.3	21.7
S_1: 100°C, 0.5 h	Cantor phase	21.05	15.23	21.55	20.76	21.40
S_2: 100°C, 2 h	Cantor phase	20.94	15.36	21.46	20.75	21.49
S_3: 150°C, 1 h	Cantor phase	20.87	16.22	21.80	20.52	20.59
S_4: 200°C, 1 h	Cantor phase	20.71	15.53	21.77	20.89	21.10
S_5: 250°C, 1 h	Cantor phase	20.99	12.81	22.00	21.90	22.30
S_6: 300°C* (870°C 10 min + 800°C 50 min)	remaining Cantor phase	22.29	13.30	21.59	21.53	20.67
	B2	4.91	3.05	43.60	38.94	9.04
	$L1_0$	1.67	26.75	10.76	13.73	47.10
	σ	46.94	7.30	14.80	25.31	8.59
	bcc	71.00	0.92	11.10	10.60	5.53
S_7: 350°C, 1 h	B2	3.18	4.06	49.62	35.91	7.40
	$L1_0$	12.83	15.78	16.41	13.64	43.93
	σ	50.37	1.51	15.13	21.41	11.60
	bcc	76.55	1.41	10.28	7.34	4.44

Table 2. Measured d-spacings from the electron diffraction data and corresponding crystallographic planes (h k l) of the identified phases. The annotation DR given next to the hkl refers to diffuse diffraction ring. The given deviation represents the difference between the measured and the ICSD values. Newly appearing diffraction rings are highlighted in red.

Temp. (Fig.)	d-spacing [nm]	(h k l) Phase [Deviation]
S_0: as-deposited (Supplementary Fig. 2a, 6a	0.204	(111)$_{DR}$ Cantor phase [-1.9%]
	0.121	(022)$_{DR}$ Cantor phase [-4.7%]
	0.104	(311)$_{DR}$ Cantor phase [-4.6%
S_0: as-deposited (Supplementary Fig. 2b)	0.202	(111) Cantor phase [-2.9%]
S_1: 100°C (Supplementary Fig. 6b)	0.204	(111)$_{DR}$ Cantor phase [-1.9%]
	0.121	(022)$_{DR}$ Cantor phase [-4.7%]
	0.104	(311)$_{DR}$ Cantor phase [-4.6%]
S_3: 150°C (Supplementary Fig. 6c)	0.204	(111)$_{DR}$ Cantor phase [-1.9%]
	0.120	(022)$_{DR}$ Cantor phase [-5.5%]
	0.104	(311)$_{DR}$ Cantor phase [-4.6%]
S_4: 200°C (Supplementary Fig. 6d)	0.204	(111)$_{DR}$ Cantor phase [-1.9%] (220)$_{DR}$ Mn_3O_4 [0.0%]
	0.143	(400) Mn_3O_4 [-0.7%]
	0.122	(022) Cantor phase [-3.9%] (404) Mn_3O_4 [-0.8%]
	0.118	(008) Mn_3O_4 [0.0%]
	0.103	(311)$_{DR}$ Cantor phase [-5.5%] (327) Mn_3O_4 [0.0%]
S_6: 250°C (Supplementary Fig. 6e)	0.251	(211) Mn_3O_4 [1.2%] (110) Cr_2O_3 [1.6%]
	0.204	(111)$_{DR}$ Cantor phase [-1.9%] (220)$_{DR}$ Mn_3O_4 [0.0%] (202)$_{DR}$ Cr_2O_3 [0.0%]
	0.143	(400) Mn_3O_4 [-0.7%] (300) Cr_2O_3 [0.0%]
	0.120	(022) Cantor phase [-5.5%] (404) Mn_3O_4 [-2.4%] (220) Cr_2O_3 [-3.2%]
	0.117	(008) Mn_3O_4 [-0.9%] (223) Cr_2O_3 [-1.7%]
	0.104	(311)$_{DR}$ Cantor phase [-4.6%] (327) Mn_3O_4 [1.0%] (21 10) Cr_2O_3 [0.0%]
S_6: 300°C* (Supplementary Fig. 6f)	0.255	(211) Mn_3O_4 [2.8%] (110) Cr_2O_3 [3.2%] (100) $L1_0$ [-2.3%] (221) σ [-1.2%]
	0.204	(111)$_{DR}$ Cantor phase [-1.9%] (220)$_{DR}$ Mn_3O_4 [0.0%] (202)$_{DR}$ Cr_2O_3 [0.0%] (011) B2 [0.5%] (101) $L1_0$ [-2.4%] (202) σ [0.0%] (111) Cr bcc [-1.9%]
	0.179	(002)$_{DR}$ Cantor [-0.6%] (105) Mn_3O_4 [0.0%] (024) Cr_2O_3 [-1.1%] (002) $L1_0$ [2.9%] (002) Cr bcc [-0.6%] (312) σ [0.0%]
	0.143	(400) Mn_3O_4 [-0.7%] (300) Cr_2O_3 [0.0%] (002) B2 [0.0%] (102) $L1_0$ [-1.4%] (432) σ [2.1%]

	0.127	(022) Cantor phase [0.0%] (404) Mn$_3$O$_4$ [3.3%] (220) Cr$_2$O$_3$ [2.4%] (012) B2 [-0.8%] (112) L1$_0$ [0.0%] (532) σ [0.0%] (022) Cr bcc [0.0%]
	0.117	(008) Mn$_3$O$_4$ [-0.6%] (223) Cr$_2$O$_3$ [-1.7%] (112) B2 [0.0%] (112) L1$_0$ [0.0%] (721) σ [0.0%]
	0.108	(311) Cantor phase [-0.9%] (503) Mn$_3$O$_4$ [0.0%] (226) Cr$_2$O$_3$ [-0.9%] (211) L1$_0$ [-2.7] (722) σ [0.9%] (113) Cr bcc [-0.9%]
	0.104	(222) Cantor phase [0.0%] (327) Mn$_3$O$_4$ [1.0%] (21 10) Cr$_2$O$_3$ [0.0%] (022) B2 [3.0%] (202) L1$_0$ [-1.0%] (821) σ [0.0%] (222) Cr bcc [0.0%]
S$_7$: 350°C (Supplementary Fig. 6g)	0.293	(200) Mn$_3$O$_4$ [1.6%] (001) B2 [2.1%] (220) σ [-6.4%]
	0.252	(211) Mn$_3$O$_4$ [2.8%] (110) Cr$_2$O$_3$ [2.0%] (100) L1$_0$ [-3.5%] (220) σ [-2.3%]
	0.205	(220) Mn$_3$O$_4$ [0.5%] (202) Cr$_2$O$_3$ [0.5%] (011) B2 [1.0%] (101) L1$_0$ [-1.9%] (202) σ [0.0%] (111) Cr bcc [-1.4%]
	0.178	(105) Mn$_3$O$_4$ [-0.6%] (024) Cr$_2$O$_3$ [-1.7%] (002) L1$_0$ [2.3%] (002) Cr bcc [-1.1%] (312) σ [0.0%]
	0.148	(400) Mn$_3$O$_4$ [2.8%] (300) Cr$_2$O$_3$ [3.5%] (002) B2 [3.5%] (102) L1$_0$ [2.1%] (432) σ [5.7%]
	0.126	(404) Mn$_3$O$_4$ [2.4%] (220) Cr$_2$O$_3$ [1.6%] (012) B2 [-1.6%] (112) L1$_0$ [-0.8%] (532) σ [-0.8%] (022) Cr bcc [-0.8%]
	0.107	(503) Mn$_3$O$_4$ [-0.9%] (226) Cr$_2$O$_3$ [-1.8%] (211) L1$_0$ [-3.6] (722) σ [0.0%] (113) Cr bcc [-1.8%]
	0.103	(327) Mn$_3$O$_4$ [0.0%] (21 10) Cr$_2$O$_3$ [-1.0%] (022) B2 [2.0%] (202) L1$_0$ [-1.9%] (821) σ [-1.0%] (222) Cr bcc [-1.0%]
350°C	0.255	(211) Mn$_3$O$_4$ [2.8%] (110) Cr$_2$O$_3$ [3.2%] (100) L1$_0$ [-2.3%]

(Fig. 5b)		(220) σ [-1.6%]
	0.206	(220) Mn_3O_4 [1.0%]
		(202) Cr_2O_3 [1.0%]
		(011) B2 [1.5%]
		(101) $L1_0$ [-1.4%]
		(202) σ [1.0%]
		(111) Cr bcc [-1.0%]
	0.183	(105) Mn_3O_4 [2.2%]
		(024) Cr_2O_3 [1.1%]
		(002) $L1_0$ [5.1%]
		(312) σ [2.8%]
		(002) Cr bcc [1.7%]
	0.150	(224) Mn_3O_4 [-2.6%]
		(214) Cr_2O_3 [2.7%]
		(321) σ [-3.2%]
350°C	0.145	(400) Mn_3O_4 [0.7%]
(Fig. 5b)		(300) Cr_2O_3 [1.4%]
		(002) B2 [1.4%]
		(400) $L1_0$ [0.0%]
		(432) σ [3.6%]
	0.128	(156) Mn_3O_4 [4.1%]
		(220) Cr_2O_3 [3.2%]
		(012) B2 [0.0%]
		(112) $L1_0$ [0.8%]
		(521) σ [0.8%]
		(022) Cr bcc [0.8%]
	0.118	(008) Mn_3O_4 [0.0%]
		(223) Cr_2O_3 [-0.8%]
		(112) B2 [0.9%]
		(211) $L1_0$ [6.3%]
		(720) σ [-2.5%]

^{DR} – diffuse ring

TEM investigations (Fig. 5, Supplementary Fig.2 and Supplementary Fig. 6) reveal stability of the nanocrystalline single phase fcc solid solution up to 250°C. After annealing at 200°C for 1 h (S_4) first additional planes appear on selected area diffractions which are identified as Mn_3O_4 (Supplementary Fig. 6d). After S_5 (250°C for 1 h) Cr_2O_3 is identified (Supplementary Fig. 6e). Further annealing at 300°C (S_6) causes decomposition of the Cantor phase into FeCo-B2, NiMn-$L1_0$, σ-phase and Cr-rich bcc phase. Separated diffraction spots on diffractions rings indicate grain coarsening after the final annealing S_7 (350°C, 1 h), see Fig. 4 and Supplementary Fig. 6.

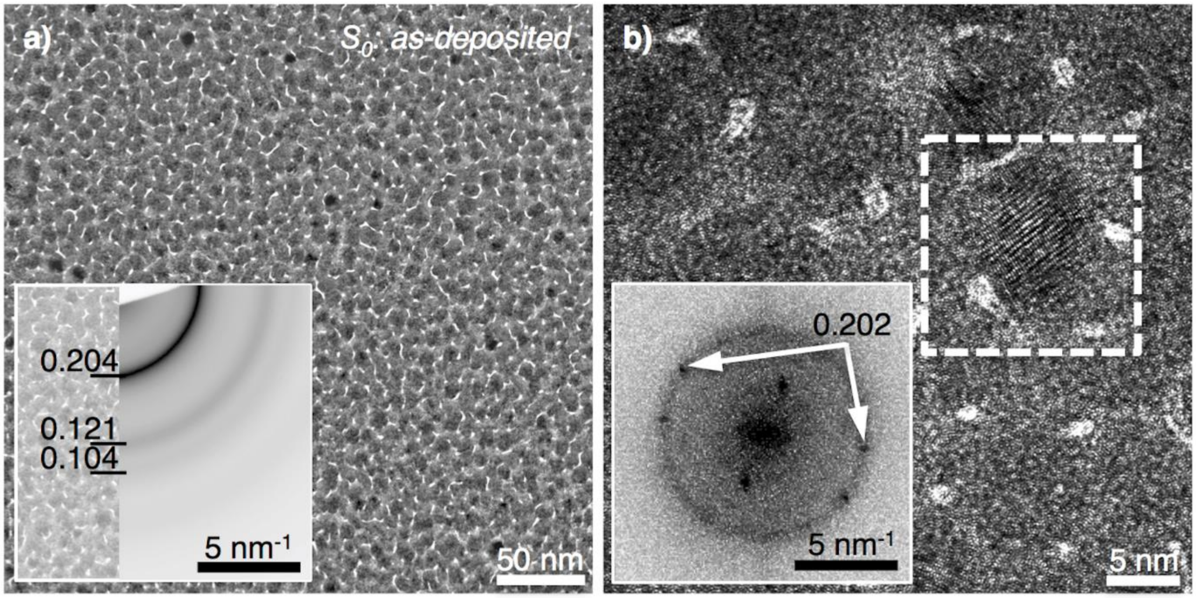

Fig. 2. TEM analyses of the microstructure of the as-deposited nanocrystalline Cantor phase on a TEM grid. a, Bright-field image with corresponding selected area diffraction showing fcc structure. b, High resolution image showing lattice fringes and the corresponding fast Fourier transformation.

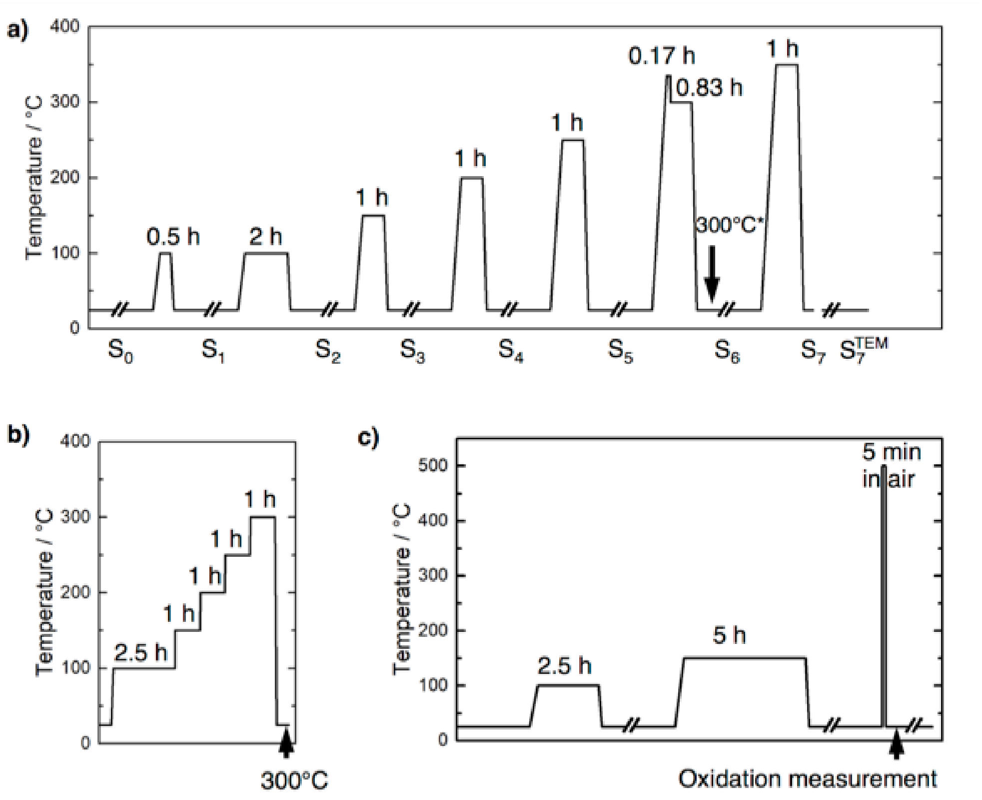

Fig. 3. CPP processing details. a, Sequential annealing up to 350°C with the corresponding state designations. b, Repetition of S_6 with continuous vacuum throughout the annealing. For APT data, see Supplementary Fig. 4c, Vacuum annealing followed by oxidation at 500 °C for 5 min in air. Breaks on the horizontal axes indicate time for APT studies after each annealing state. TEM data of the as-annealed state $S_{7,\ \mathrm{TEM}}$ is shown in Fig.4.

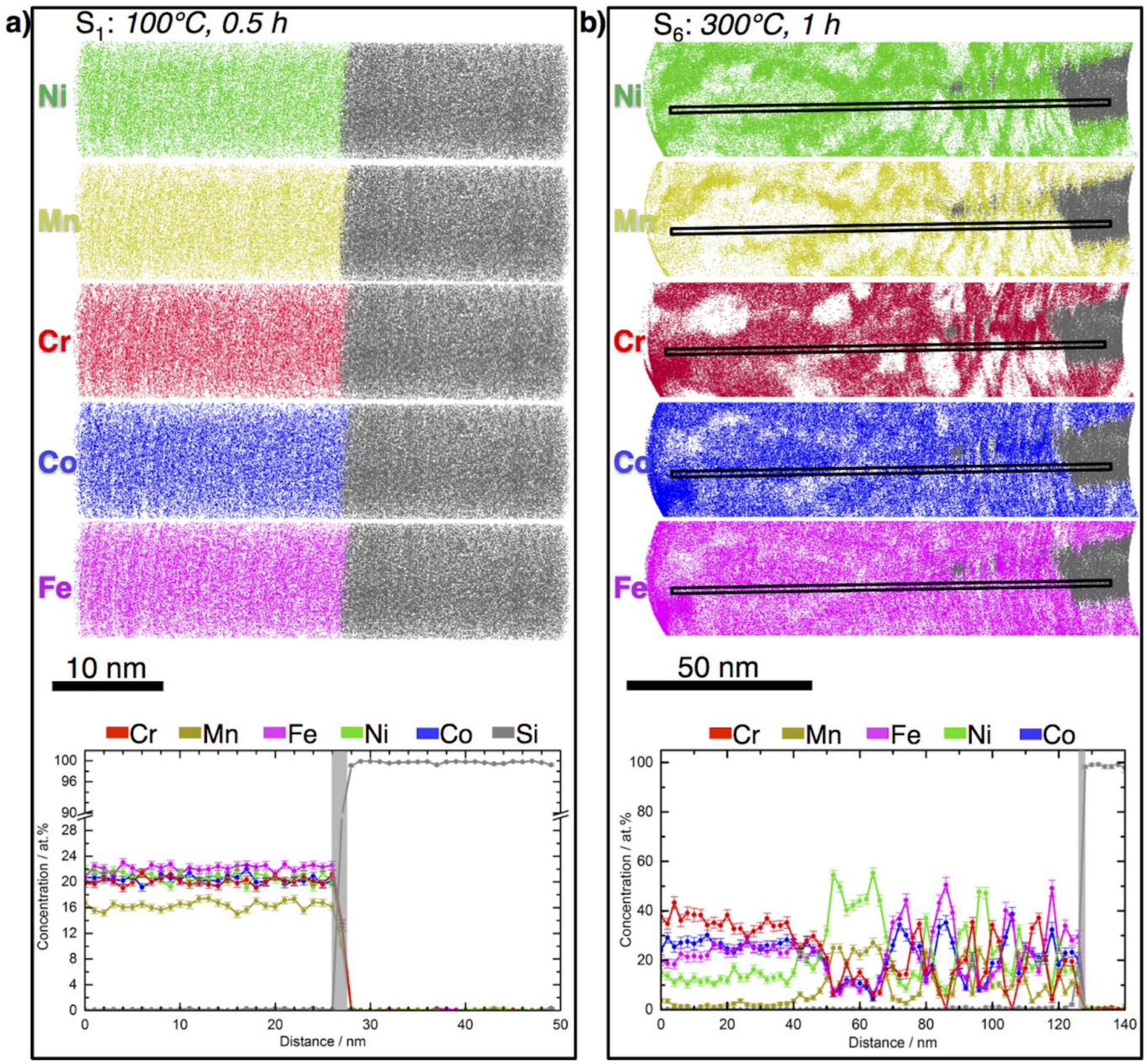

Fig. 4. Atom maps of CrMnFeNiCo thin films on Si tips. A selected volume of 12 x 12 x 50 nm^3 is shown after annealing at (a) 100°C for 0.5 h and (b) after stepwise annealing in vacuum up to 300°C (identical steps as in Table 1, however without intermediate cooling and air exposure). The atom distributions maps and the concentration profiles through the interface between the film and Si tip show that the thin film is homogeneously coated on the Si tip. There is no interdiffusion between the Si tip substrate and the metallic coating.

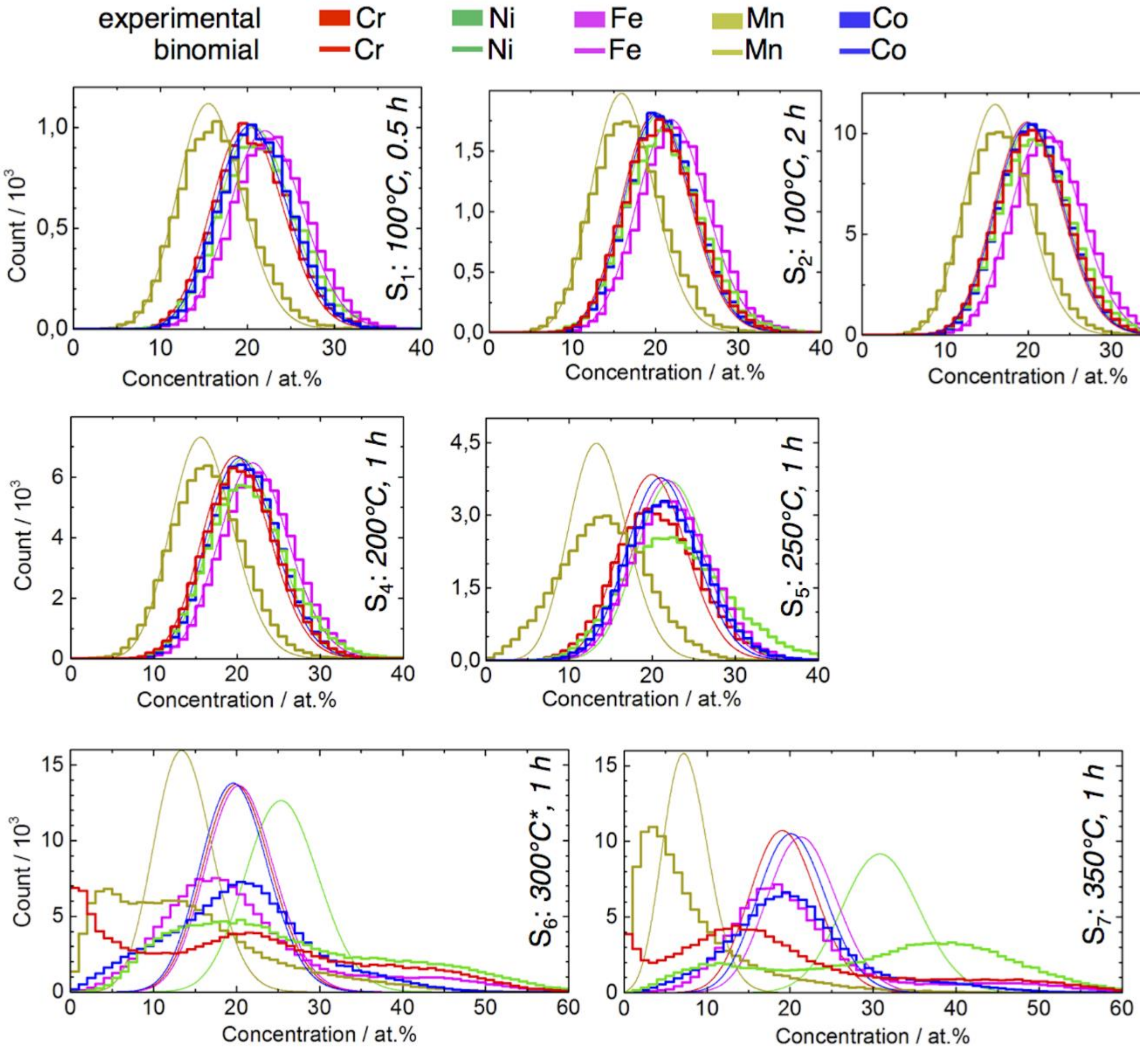

Fig. 5. Binomial frequency distribution analyses for all five elements in the detected volumes with exclusion of the Mn cap and oxide layer contained in the 2 - 3 nm-thick layer from each tip apex. Thin and thick lines represent the theoretical and measured binomial distributions, respectively. Colors for different elements are identical to the atom maps in Fig. 2. The experimental data increasingly deviates from calculated, uniform distributions with annealing temperature up to 250°C for Ni and Mn, consistent with their increasing segregation at grain boundaries (Fig. 2). Further significant shifts of the experimental from the calculated data in the states S_6 and S_7 are related to the occurrence of phase decomposition of the initial Cantor phase.

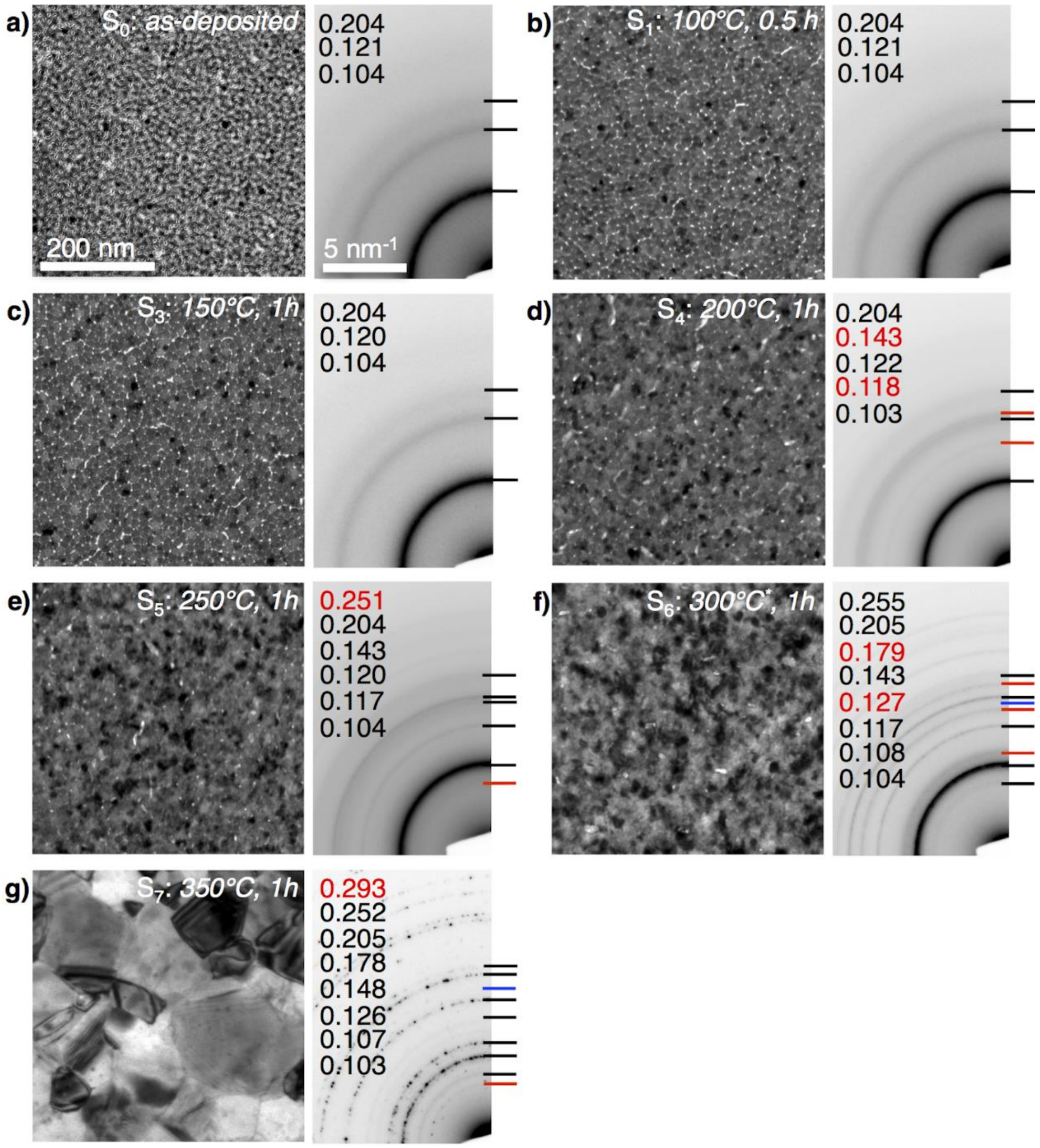

Fig. 6. TEM analyses of the microstructure evolution of a Cantor alloy film deposited on a TEM grid in different processing states: (a), S_0, as deposited; (b), S_1, 100°C, 0.5 h; (c) S_3, 150°C, 1 h; (d), S_4, 200°C, 1 h; (e), S_5, 250°C, 1 h; (f), S_6, 300°C*, 1 h; (g), S_7, 350°C, 1 h. Numbers on electron diffraction patterns correspond to measured interplanar distances in nm. Red lines indicate new interplanar distances that arise after annealing; blue indicate lines that disappeared.

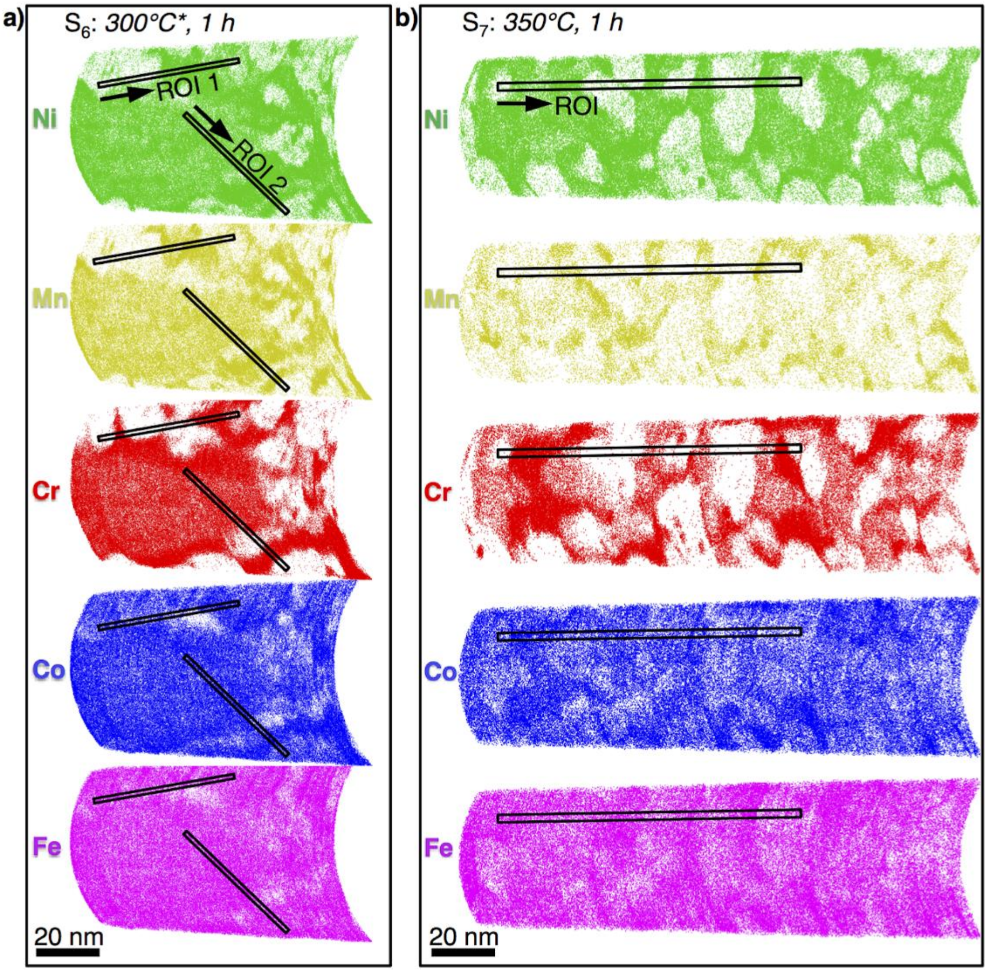

Fig. 7. Longitudinal APT element distribution maps of the decomposed Cantor phase alloy: Ni (green), Mn (yellow), Cr (red), Co (blue), and Fe (pink) within a 3 nm-thick slice after annealing at (a) in state S$_6$ and (b) S$_7$. The regions selected for concentration analyses appear also in Figs. 3a and c.

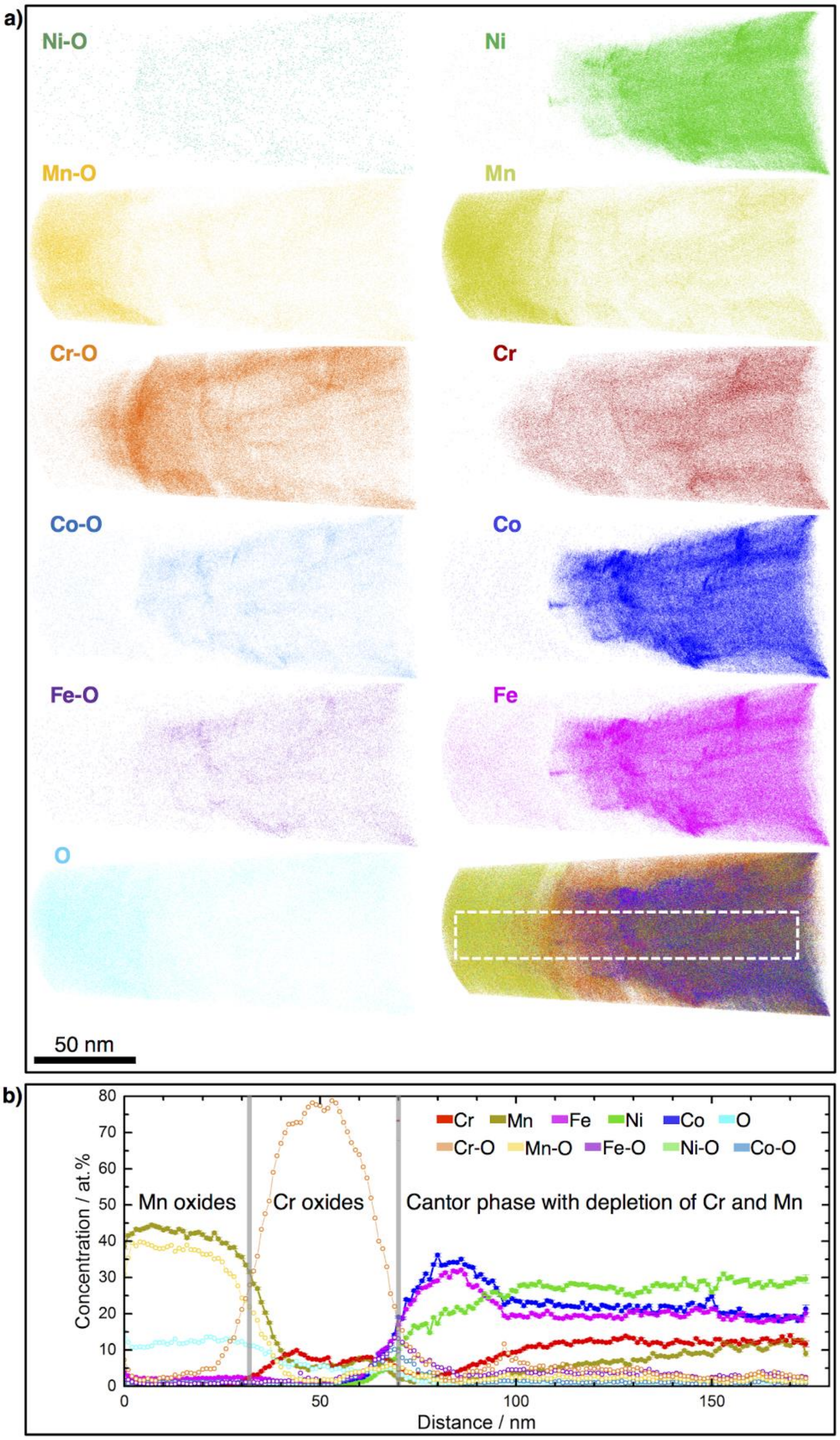

Fig. 8. APT results of the CPP oxidation experiment. (a) Atom maps of the detected O, alloy elements and their oxide species. (b) 1D concentration profiles of all detected alloy elements and their oxide species for the selected region indicated in (a).

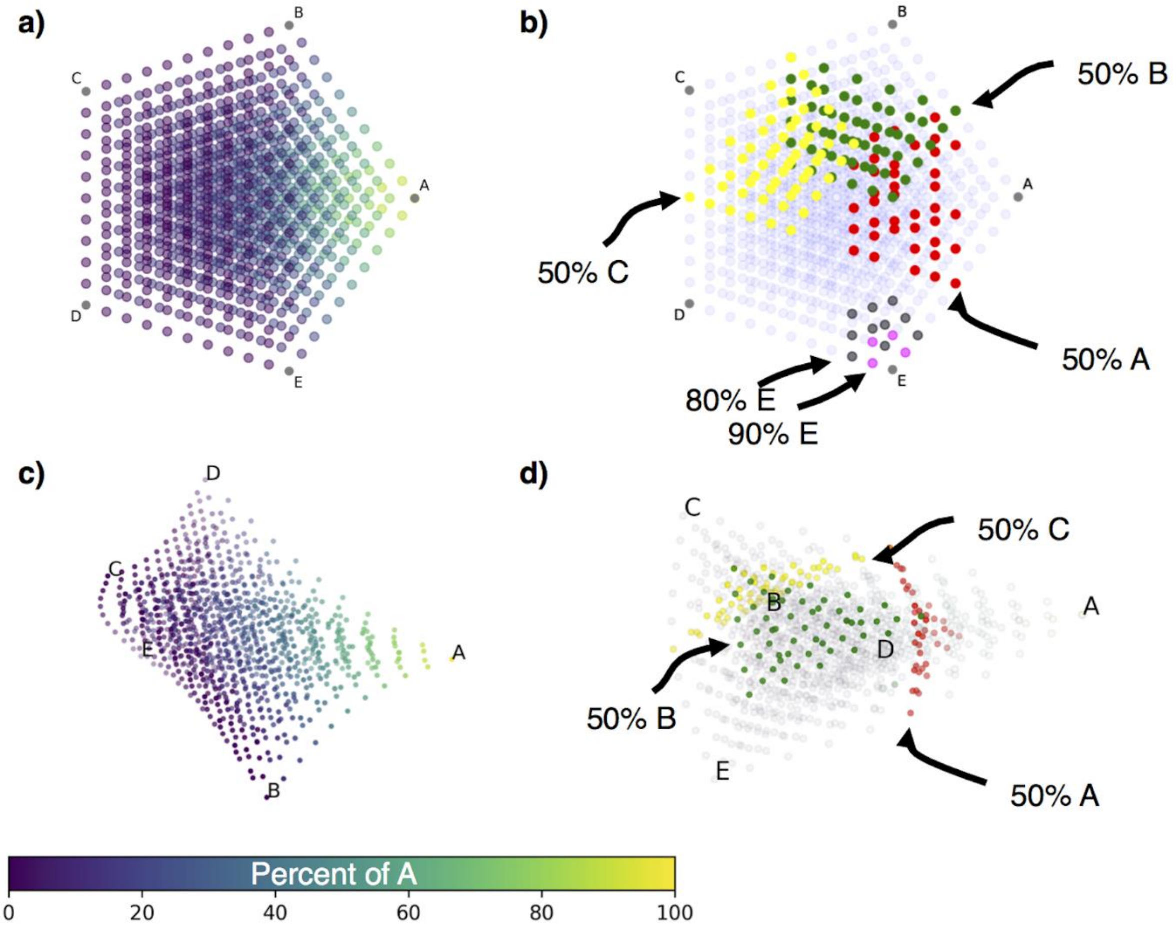

Fig. 9. Comparison of RadViz and MDS visualization. (a) RadViz visualization with the color-coded A content. As is visible from this graph compositions with very different composition overlap. (b) Iso-elemental sections of 50 % for A, B, C these regions visually overlap and change shape with concentration as shown for the representative sections for E = 80%, 90%. (c) MDS visualization with the color-coded A content. As is visible from this graph points with the same content of A lie mostly on a plane describing an equal distance from A. Some points do not fall onto this plane due to (mathematically unavoidable) imperfect convergence of the MDS. (d) View angle highlighting the iso-elemental sections of 50 % for A, B and C while looking onto that for C. Depending on the view angle, these planes do not overlap visually.

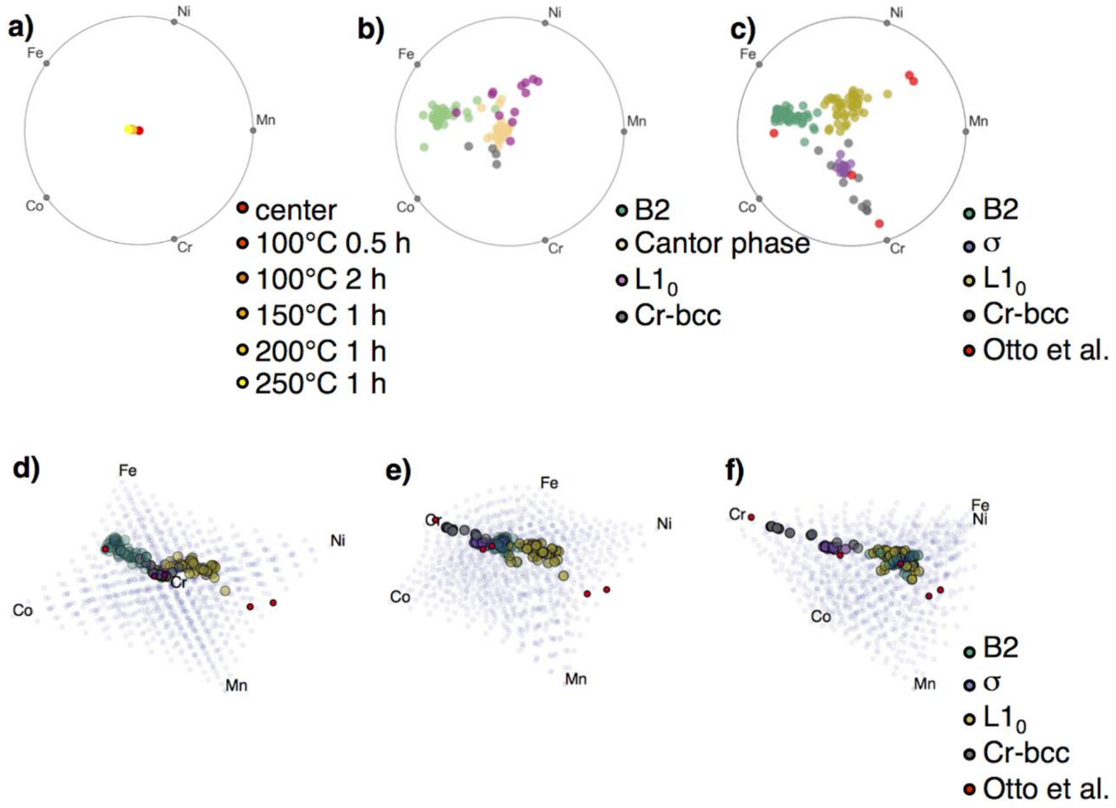

Fig. 10. Visualizations of multidimensional composition data. (a-c) RadViz visualization of the composition data from Figure 6a-c. (d-f) View angles in MDS visualization indicating the decomposition path along (d) $(FeCo)_{1-x}$-$(NiMn)_x$ and (e-f) $(FeCo)_{1-x}$-Cr_x**.** All view angles highlight that most determined phases occur compositionally close to those found in the bulk study[11] after > 500 d of annealing.

Video of MDS visualization

see additional file

References (1-*25*)

1. Z. Li, K. G. Pradeep, Y. Deng, D. Raabe and C. C. Tasan, *Nature*, 2016, **534**, 227–230.
2. B. Gludovatz, A. Hohenwarter, K.V.S. Thurston, H. Bei, Z. Wu, E. P. George and R. O. Ritchie, *Nature Commun*., 2016, **7**, 10602.
3. B. Gludovatz, A. Hohenwarter, D. Catoor, E. H. Chang, E. P. George and R. O. Ritchie, *Science,* 2017, **345**, 1153-1158.
4. S. Curtarolo, G. L. W. Hart, M. B. Nardelli, N. Mingo, S. Sanvito and O. Levy, *Nature Mater.*, 2013, **12**, 191-201.
5. X. D. Xiang, X. Sun, G. Briceho, Y. Lou, K. Wang, H. Chang, W. G. Wallace-Freedman, S. Chen and P. G. Schultz, *Science*, 1995, **268**, 1738-1740.
6. D. B. Miracle and O. N. Senkov, *Acta Mater*., 2017, **122**, 448-511.
7. G. Schmitz, C. B. Ene and C. Nowak, *Acta Mater., 2009*, **57**, 2673-2683.
8. C. B. Ene, G. Schmitz, R. Kirchheim and A. Hütten, *Acta Mater*., 2005, **53**, 3383-3393.
9. T. Jeske and G. Schmitz, *Mater. Sci. Eng. A*, 2002, **327**, 101-108.
10. B. Cantor, I. T. H. Chang, P. Knight and A. J. B. Vincent, *Mater. Sci. Eng.* A, 2004, **375-377**, 213-218.
11. F. Otto, A. Dlouhý, K.G. Pradeep, M. Kubenova, D. Raabe, G. Eggeler and E.P. George, *Acta Mater*., 2016, **112**, 40-52.
12. B. Schuh, F. Mendez-Martin, B. Völker, E.P. George, H. Clemens, R. Pippan and A. Hohenwarter, Mechanical properties, *Acta Mater*., 2015, **96,** 258-268.
13. R.Z. Valiev, R.K Islamgaliev and I.V. Alexandrov, *Prog. Mater. Sci.*, 2000, **45**, 103-189.
14. B. B. Straumal, B. Baretzky, A. A. Mazilkin, F. Phillipp, O. A. Kogtenkova, M. N.Volkov and R.Z. Valiev, *Acta Mater*., 2004, **52,** 4469-4478.
15. D. Sata, K. Ebermann, K. Eberl and J. Maier, *Nature*, 2000, **408,** 946-949.
16. R. Würschum, S. Herth and U. Brossmann, *Adv. Eng. Mat*., 2003, **5**, 365-372.
17. G. Laplanche, U. F. Volkert, G. Eggeler and E. P. George, *Oxid. Met.*, 2016, **85**, 629-645.
18. C. Suh, S. C. Sieg, M. J. Heying, J. H. Oliver, W. Maier and K. Rajan, 2009, **11(3)**, 385-392.
19. A. Ludwig, R. Zarnetta, S. Hamann, A. Savan and S. Thienhaus, *Int. J. Mat. Res*., 2008, **99,** 1144-1149.
20. B. Gault, M. P. Moody, J. M. Cairney and S. P. Ringer, *Atom Probe Microscopy* (Springer, 2012).
21. G. Laplanche, P. Gadaud, O. Horst, F. Otto, G. Eggeler and E.P. George, *J. Alloy. Compd.*, 2015, **623**, 348-353.
22. J. B. Kruskal, *Psychometrika*, 1964, **29**, 115-129.
23. F. Pedregosa, G. Varoquaux, A. Gramfort, V. Michel, B. Thirion, O. Grisel, M. Blondel, P. Prettenhofer, R.Weiss, V. Dubourg, J. Vanderplas, A. Passos, D. Cournapeau, M. Brucher, M. Perrot and E. Duchesnay, *Journal of Machine Learning Research*, 2011, **12**, 2825-2830.